Geophysical Research Letters

RESEARCH LETTER
10.1029/2021GL093664

Field Observations of the Evolution of Plunging-Wave Shapes

Annika O'Dea[1,2], **Katherine Brodie**[1], **and Steve Elgar**[3]

[1]Coastal & Hydraulics Laboratory, U.S. Army Engineer Research and Development Center, Duck, NC, USA, [2]Oak Ridge Institute for Science and Education, Oak Ridge, TN, USA, [3]Woods Hole Oceanographic Institution, Woods Hole, MA, USA

Key Points:

- Three-dimensional lidar scans of the water surface allow for quantitative analyses of the shape and evolution of plunging breakers
- The observed internal void shapes in plunging breakers agree well with theoretical void shapes at the onset of breaking
- The internal void shape and normalized area are influenced by bathymetry, wave parameters, and cross-crest wind stress

Correspondence to:
A. O'Dea,
annika.odea@gmail.com

Citation:
O'Dea, A., Brodie, K., & Elgar, S. (2021). Field observations of the evolution of plunging-wave shapes. *Geophysical Research Letters*, *48*, e2021GL093664. https://doi.org/10.1029/2021GL093664

Received 31 MAR 2021
Accepted 13 JUL 2021

Abstract There are few high-resolution field observations of the water surface during breaking owing to the difficulty of collecting spatially dense measurements in the surf zone, and thus the factors influencing breaking-wave shape in field conditions remain poorly understood. Here, the shape and evolution of plunging breakers is analyzed quantitatively using three-dimensional scans of the water surface collected at high spatial and temporal resolution with a multi-beam terrestrial lidar scanner. The observed internal void shapes in plunging breakers agree well with previously developed theoretical shapes at the onset of breaking, and become more elongated and less steep as breaking progresses. The normalized void area increases as the local bottom slope steepens and as the breaking depth decreases. The void shape becomes more circular as the local bottom slope and the ratio of breaking water depth to wavelength increase, as well as in conditions with opposing winds.

Plain Language Summary Breaking waves inject momentum into the surf zone that drives nearshore currents, raises water levels, and generates turbulence. However, there are few high-resolution field observations of the water surface during breaking because of the difficulty of collecting spatially dense measurements of the water-surface elevation at the location of wave breaking, leaving open questions related to the factors controlling the shape and properties of breaking waves. In this study, three-dimensional scans of the water surface in the surf zone collected using a multi-beam terrestrial lidar scanner are used to analyze quantitatively the shape and evolution of plunging breakers. The shape of the internal barrel (or void) created as the plunging lip intersects with the front face of the wave agrees well with theoretical void shapes at the start of the breaking process, and then becomes more elongated and less steep through the breaking process. The normalized area of the void is larger when waves break on steeper bottom slopes and in shallower water. The void is more circular when waves break on steeper bottom slopes and with larger ratios of breaking water depth to wavelength, and also when the wind is blowing in a direction opposing the direction of wave propagation.

1. Introduction

Depth-induced wave breaking transfers momentum into the surfzone water column, driving cross- and alongshore currents, increasing shoreline water levels, and generating turbulence and vorticity (Peregrine, 1998). Breaking waves often are categorized based on their shapes and properties, with plunging and spilling breakers the primary types on most beaches (Galvin, 1968; Peregrine, 1983; Battjes, 1988). Plunging breakers are characterized by the formation of an internal air cavity (or void) as the crest of the wave curls forward and connects with the wave face. This void eventually collapses, dissipating energy, generating turbulence, and entraining air bubbles (Kiger & Duncan, 2012; Peregrine, 1983). Relative to spilling breakers, plunging breakers generate high levels of turbulence that extend deeper in the water column (Flick et al., 1981; Ting & Kirby, 1994, 1995, 1996; Aagaard et al., 2018) and increase suspended sediment concentrations (Aagaard et al., 2018; Beach & Sternberg, 1996; Inman et al., 1980; Nielsen, 1984; Voulgaris & Collins, 2000).

Observing the rapid transformation of the shapes of waves as they shoal and begin to break requires spatially dense measurements in and near the surf zone, which are difficult to obtain in the field, particularly in high-energy, plunging conditions. Most studies focusing on the shape of depth-limited plunging breakers have utilized laboratory experiments (Blenkinsopp & Chaplin, 2007, 2008; Chanson & Jaw-Fang, 1997;

Ting & Kirby, 1994, 1995; Yasuda et al., 1997) or numerical simulations (Grilli & Svendsen, 1990; Grilli et al., 1997, 2001; Lin & Liu, 1998; Lubin et al., 2006; Vinje & Brevig, 1981; Yasuda et al., 1997), many of which are extensions of earlier numerical and parametric studies focused on deep-water plunging wave shapes (Longuet-Higgins, 1982; Longuet-Higgins & Cokelet, 1976, 1978; Peregrine et al., 1980).

A depth-independent parametric form of the equations of motion (Longuet-Higgins, 1982) has been used to assess depth-limited plunging wave shapes in the laboratory (Blenkinsopp & Chaplin, 2008) and the field (Mead & Black, 2001). In these studies, a modified curve was fit to optical images of breaking waves, and the resulting curve parameters were used to characterize the plunging wave shapes, and to analyze the factors contributing to the differences between observed and theoretical shapes. However, the field study (Mead & Black, 2001) provided only limited quantitative analysis owing to the use of unrectified optical snapshots during breaking and the lack of spatially and temporally overlapping wave and environmental data. The factors controlling plunging-wave shapes in field conditions, and thus their contribution to nearshore circulation, air-sea gas exchange, and sediment transport, remain poorly understood.

Here, the shape and evolution of plunging waves in the field are analyzed quantitatively using a novel multi-beam lidar collection approach that produces three-dimensional scans of the water surface at high spatial and temporal resolution. The shape of the internal void in finite-crested plunging waves is reconstructed by combining information from multiple beams surrounding the leading edge of the breaking crest. This multi-beam system allows the dual free surface formed by the plunging lip to be measured, which is not possible with two-dimensional lidar scanners used previously (Blenkinsopp et al., 2010; Brodie et al., 2015; Martins et al., 2017, 2018) owing to the shadowing that occurs from the plunging lip when measured along a single transect. For each wave, the shape of the internal void created by the plunging lip is compared with theory (Longuet-Higgins, 1982), and the spatio-temporal evolution of the plunging wave and the factors influencing the void shape, angle from horizontal, and area are assessed at the onset of breaking.

2. Methods

2.1. Observations

Breaking-wave shapes were determined from three-dimensional lidar scans of the water surface collected at the U.S. Army Engineer Research and Development Center's Field Research Facility (FRF) on the Atlantic coast of North Carolina. A Velodyne HDL-32E lidar scanner was mounted on a horizontal arm attached to a platform on an amphibious vehicle (CRAB) (Birkemeier & Mason, 1984), enabling unobstructed views of the water surface (Figure 1a). The lidar simultaneously emits 32 beams (903 nanometer wavelength) that each scan along a single line in space. The lidar returns provide the location (distance and angles, converted to Cartesian coordinates) where each beam intersects the water, creating a three-dimensional snapshot of the surface with a typical accuracy of up to ±0.02 m. The beams are spaced at 1.33° increments resulting in a 41.34° field of view. The alongshore extents of the scans thus increase with distance from the scanner from ~7 m (below the scanner) to ~20 m (~±25 m cross-shore from the scanner). The azimuthal (cross-shore) resolution is a function of the adjustable speed of rotation (10 Hz here) and the fixed firing time (46.08 μs), resulting in a resolution of 0.166°. The cross-shore extent of quality returns depends on the water surface roughness, foam, and sediment concentrations, and often was less than the effective terrestrial range (100 m). During post-processing, the scans were limited to a 60- × 25-m cross- and alongshore range, although most scans extended 30–50 m in the cross-shore and up to 15 m in the alongshore direction (Figure 1c).

Scans were collected for eight 30-min periods during conditions with plunging breakers on September 7, September 8, and October 25, 2017. The CRAB was positioned near the surfzone break point (Figure 1a) for each collection period, and relocated after each 30-min period to account for changes in wave-breaking location owing to changing wave conditions and water levels (circles in Figure 1b). The cross-shore position of the CRAB varied up to 75 m over the collection periods. The alongshore location of the CRAB was approximately fixed on each of the three days, but varied up to 632 m between days. On each day of data collection the bathymetry was surveyed along a cross-shore transect from the dune to ~5-m water depth (mean cross-shore resolution ~0.7 m) at the alongshore location of the CRAB (Forte et al., 2017) (Figure 1b).

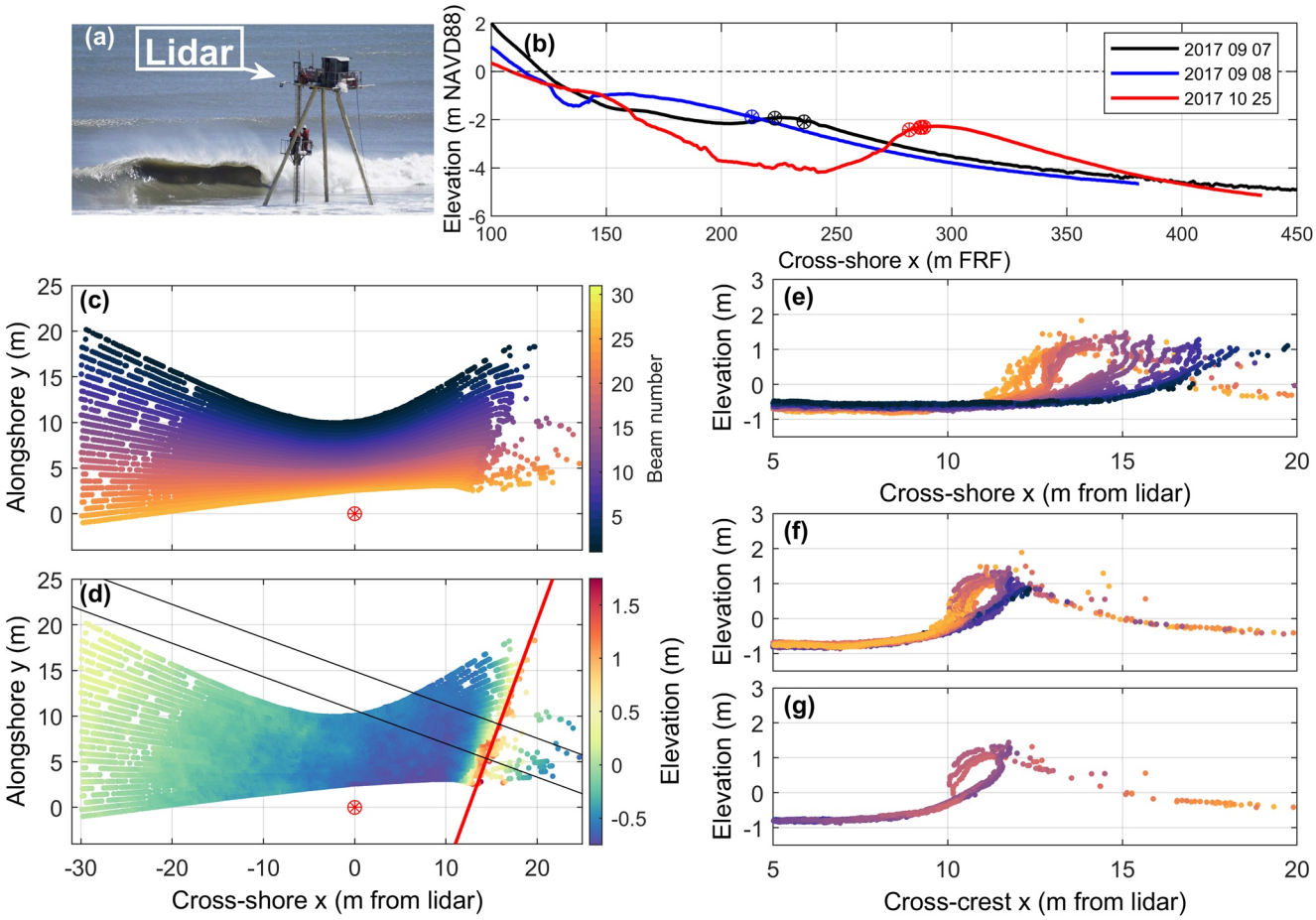

Figure 1. (a) The CRAB sampling platform and (b) seafloor elevation (relative to NAVD88) versus Field Research Facility cross-shore coordinate measured on the three days of data collection. The circles in panel (b) indicate the location of the CRAB for each collection period, with three locations on September 7 (black), one on September 8 (blue), and four on October 25 (red), and with colors corresponding to the day of collection. (c), (d) An example lidar scan shown in alongshore versus cross-shore coordinates (relative to the lidar location, indicated with a red circle, and with the positive *x*-axis increasing offshore), colored by (c) beam number and (d) elevation, (e) sea-surface elevation versus cross-shore coordinate, and (f), (g) sea-surface elevation versus cross-crest coordinate (where the *x*-axis is orthogonal to the wave crest), showing (f) the whole scan and (g) only points within a 4-m along-crest window, indicated with parallel black lines in panel (d). Points in panels (e)–(g) are colored by beam number. The thick red line in panel (d) shows the angle of the wave crest relative to shore parallel used to generate the cross- and along-crest coordinate system.

All scans within each 30-min collection period were transformed into a local, globally aligned, lidar-centric coordinate system. The roll and pitch components of the transformation were determined by leveling the returns from the water surface, neglecting any small tilts due to setup or setdown. The location and yaw orientation of the lidar were determined using the known orientation of the arm on which the lidar was mounted relative to the body of the CRAB, combined with the GPS coordinates of the four corners of the CRAB, which were visible in the lidar scans. To account for the changes in the lidar orientation and location resulting from the occasional settling of the CRAB into the sediment (up to 0.3 m during the 30-min collections), the water surface was leveled using approximately 1.5 min of lidar data centered on each wave of interest. The mean water-surface elevation over that period was set to the elevation measured every 6 min at the end of the FRF pier in approximately 8-m water depth (blue curves in Figures 2g and 2h). Individual waves were identified using a zero-up-crossing technique within the region directly below the scanner.

Nearshore hydrodynamic conditions were determined from a 16-element array of bottom-mounted pressure gauges located in ~8-m water depth, which provided hourly estimates of frequency-directional wave spectra (Long & Oltman-Shay, 1991), significant wave height H_s (4 times the standard deviation of sea-surface elevation fluctuations), peak wave period T_p, and the mean wave direction at the peak frequency θ_p (Figure 2). Wind speeds and directions were measured at 1 Hz at the end of the FRF pier, and were rotated

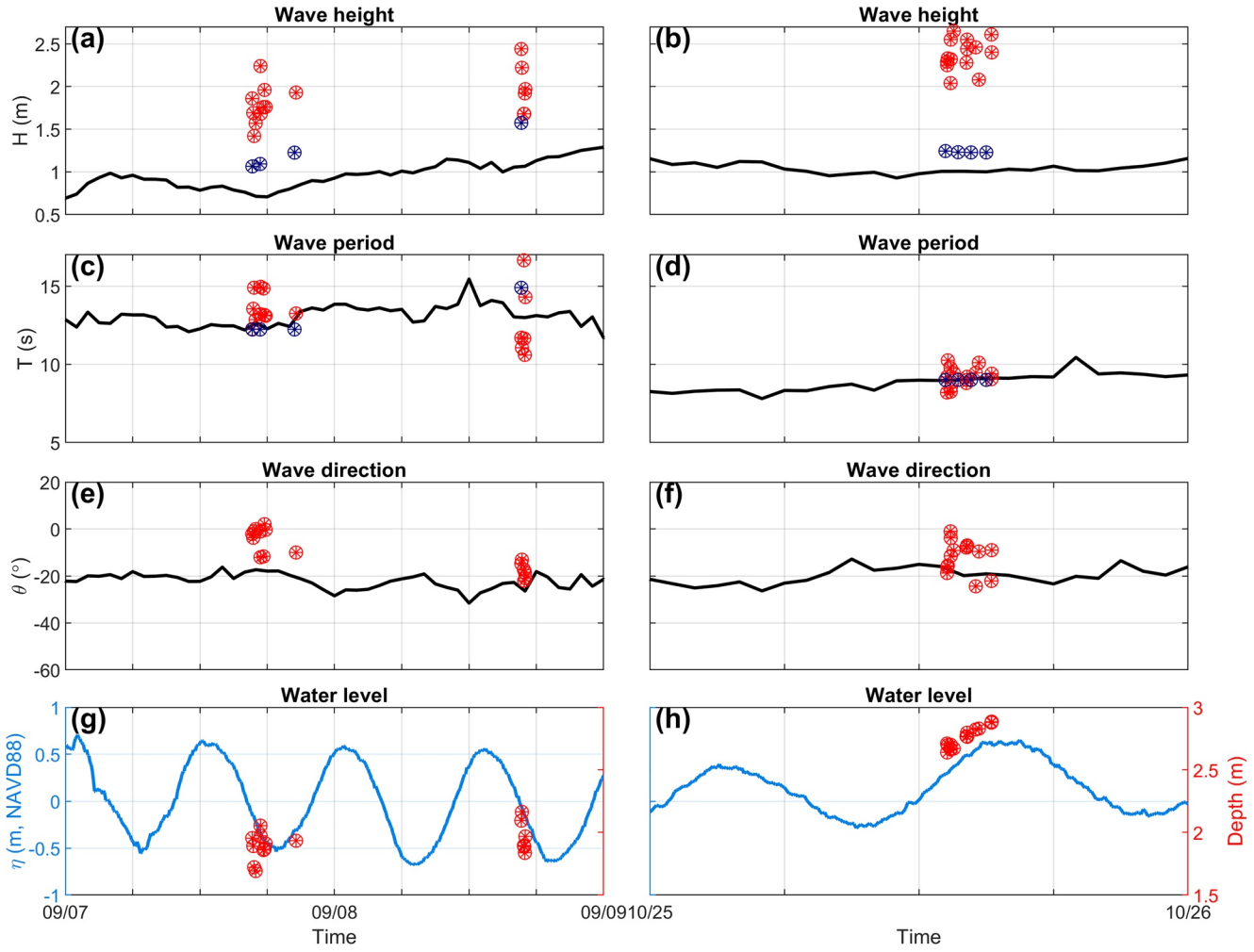

Figure 2. Time series of (a), (b) H_s; (c), (d) T_p; and (e), (f) θ_p from the 8-m array (black curves) and (g), (h) tidal elevation at the end of the Field Research Facility pier (blue curves) for the three days of data collection, with September 7–8 shown in the left panels and October 25 shown in the right panels. Blue circles in panels (a–d) show the same parameters determined from a 30-min time series of mean water-surface elevation from the lidar scans. Red circles in panels (a–f) show the wave-by-wave parameters extracted from the lidar scans and red circles in (g), (h) show the water depth at the location of wave breaking for each wave analyzed.

into a wave-oriented coordinate system (described in Section 2.2.1). Wind stress τ_w was estimated following Large and Pond (1981).

2.2. Lidar Analysis

2.2.1. Plunging Wave Identification

Lidar observations of finite-crested plunging waves enable reconstruction of the shape of the internal void by combining information from multiple beams surrounding the leading edge of the breaking crest (Figures 1f and 1g). A total of 30 plunging waves with at least three consecutive frames with clearly defined internal voids were identified manually. For each plunging wave, the angle of wave propagation within the lidar field of view was determined (Figure 1d, red line), and all scans within that wave were rotated into a wave-oriented coordinate system where the y-axis is parallel to the wave crest and the x-axis is parallel to the direction of wave propagation. The angle was estimated by finding the mean rotation angle about the z-axis in several frames that minimized the vertical spread of the water surface in $x - z$ space. This rotation collapses lidar returns on top of each other in the along-crest direction, creating a cross-crest transect of water-surface elevation when viewed in $x - z$ space (Figures 1f and 1g). To minimize the effect of alongshore

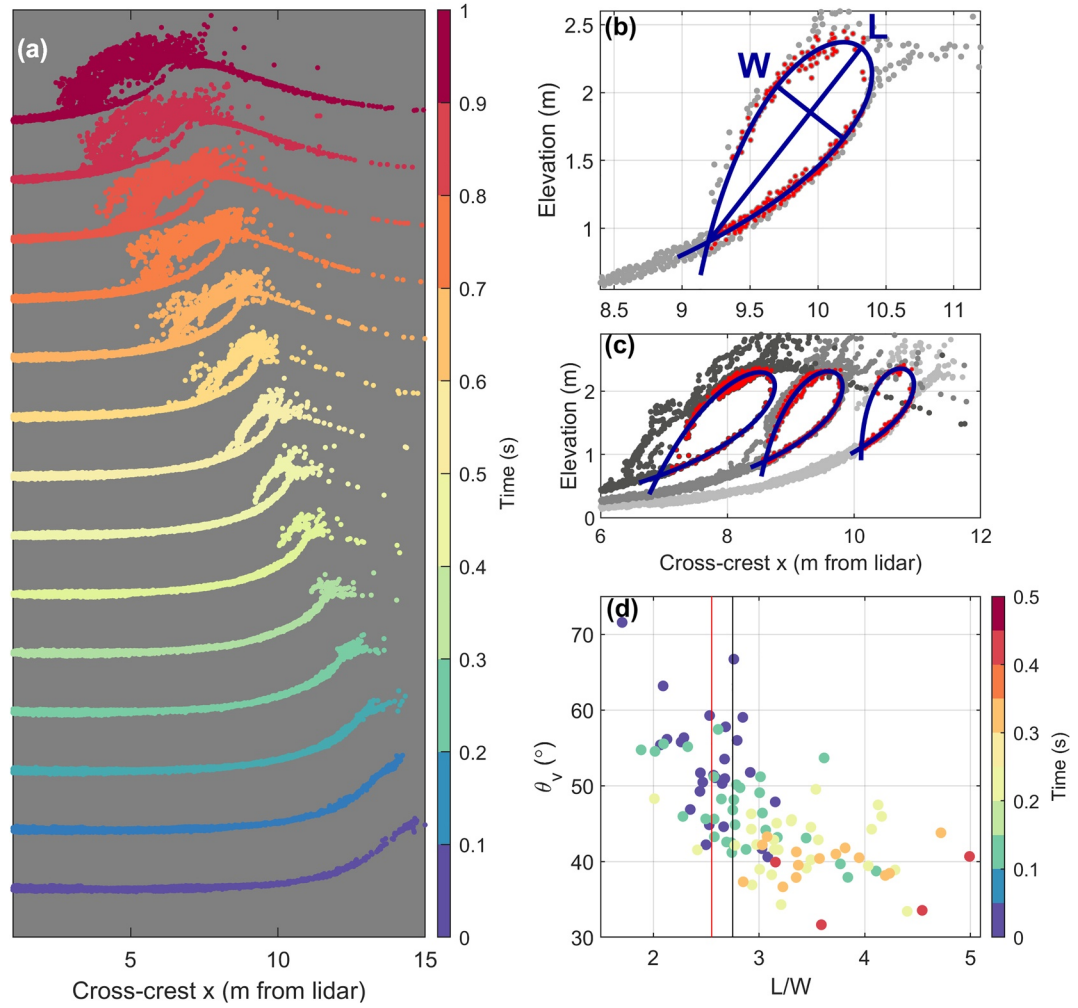

Figure 3. Sea-surface elevation versus cross-crest location for (a) lidar scans from October 25, 2017 spanning 1 s at 10 Hz (each color indicates a subsequent frame, with the time given by the color bar on the right), (b) a single scan with the function fit (blue curve, with the void length L and width W indicated), (c) three scans, each spaced 0.2 s apart with the corresponding fits (blue curves), and (d) void angle from horizontal θ_v versus void aspect ratio L/W, with dots colored by time since the closing of the void. Vertical lines show the theoretical aspect ratio (black) (Longuet-Higgins, 1982) and the mean measured aspect ratio at the time step closest to the closing of the void t_o (red). Red dots in (b), (c) show the points used to fit the function, gray dots are discarded returns.

variability on wave shape, an along-crest window centered on the leading edge of the breaking crest (3–4 m along the wave) was determined manually for each wave (Figure 1d, black parallel lines), and only points within this window were used in the analysis of the evolution of void shapes (Figure 1g).

2.2.2. Void Fitting

To characterize the plunging-wave shapes, a curve adapted from a parametric solution to the equations of motion (Longuet-Higgins, 1982) was fit to the lidar data:

$$\frac{z'}{W} = \pm\frac{3\sqrt{3}}{4}\sqrt{\frac{x'}{L}}\left(\frac{x'}{L} - 1\right) \tag{1}$$

where L and W are the length and width of the internal void in the plunging breaker, respectively, and the x-axis aligns with the major axis of the function (Blenkinsopp & Chaplin, 2008) (Figure 3b). This adapted equation is a solution to the parametric equations of motion only when the aspect ratio (L/W) is 2.76 (Longuet-Higgins, 1982). However, similar to prior work (Blenkinsopp & Chaplin, 2008; Mead &

Black, 2001), L and W were allowed to vary independently, allowing comparisons of field observations with the theoretical aspect ratio. In addition, Equation 1 provides a framework to describe the void shape quantitatively, and to compare void shapes through the breaking process and for a range of waves. Equation 1 was fit to the points on the inside edge of the internal void in each frame with a clearly defined void (3–5 frames per wave) by solving a nonlinear minimization problem using a variant of the simplex method. To extract the points on the inside edge of the void, the function was fit to all points within manually determined x and z bounds. Points greater than 0.1 m above or below the function were discarded, and the process was repeated (Figures 3b and 3c). For each fit, the resulting void length L, width W, aspect ratio L/W, angle from horizontal (i.e., the vertical angle between the major axis of the curve and the cross-crest x-axis) θ_v, and area A were calculated, with A determined from (Blenkinsopp & Chaplin, 2008)

$$A = \frac{2\sqrt{3}}{5} LW \tag{2}$$

The function given by Equation 1 and the aspect ratio (2.76) describe the moment when the curling lip of the plunging wave first intersects the front face of the wave, creating a closed void. The frame closest in time to the closing of the void (t_o) was determined for each wave, and all parameters calculated from that frame are indicated with a subscript ($_o$). In 3 of 30 waves the function could not be fit to the void at t_o due to spray or other noise. These waves are not included in the analyses of parameters at t_o.

2.2.3. Wave-By-Wave Parameters

To assess sources of variability in observed void shapes, void parameters at t_o were compared with wave and environmental parameters. Local bulk parameters (significant wave height H_s and peak period T_p, blue circles in Figures 2a–2d) over the 30-min collection periods were determined from a time series of the mean water-surface elevation over a 0.2 m (cross-shore) × 1.0 m (alongshore) rectangle directly below the lidar. Wave-by-wave parameters including breaking wave height H_b, period T_b, direction θ_{wb} (red circles in Figures 2a–2f) and speed C_b were estimated from the lidar scans. The breaking location for each wave was determined manually and defined as the location of the wave crest in the first frame that showed the crest starting to curl forward. The wave height at breaking H_b was estimated from the frame immediately prior to the initiation of breaking by finding the vertical difference between the maximum elevation of the crest (excluding spray) and the preceding minimum elevation. The period T_b was estimated as the average time between three successive wave crests centered on the breaking wave. The angle θ_{wb} was estimated during the data rectification and processing (Section 2.2.1). The wave speed C_b was estimated from the mean displacement of the wave crest from the time the wave initially enters the field of view until the internal void begins to collapse and a wave crest cannot be defined (at least 18 frames). The breaking wavelength λ_b was calculated using the lidar-derived T_b and C_b (with $\lambda_b = C_b T_b$), and was used to calculate the breaking wavenumber $k_b = 2\pi / \lambda_b$. The deep-water wavelength λ_{dw} was calculated using the linear wave theory relationship $\lambda_{dw} = gT^2 / 2\pi$. The bottom slope β_b was defined individually for each wave as the mean seafloor slope from the location of breaking to one half of a wavelength offshore, with the depth at breaking h_b defined as the mean water depth over the same area (red circles in Figures 2g and 2h). The estimated cross-crest wind stress τ_w was averaged over 20 s centered on the time of breaking.

Void parameters were compared with individual wave and environmental parameters (H_b, T_b, θ_{wb}, C_b, k_b, H_b/λ_b, β_b, h_b, and τ_w), as well as parameters combining wave and bathymetric characteristics ($\beta_b/(H_b/\lambda_b)^{1/2}$, $\beta_b(H_b/\lambda_b)^{1/2}$, and $\beta_b(k_b h_b)^{1/2}$).

3. Results and Discussion

The breaking heights H_b (red circles, Figures 2a and 2b) of each wave, as well as bulk, 30-min local (blue circles in Figures 2a and 2b) and offshore (black curves in Figures 2a and 2b) significant wave heights H_s for every collection period were estimated from the lidar scans and the array in 8-m depth, respectively. The significant wave height H_s at the location of the lidar was larger than H_s in 8-m depth due to the conservation of energy flux as the waves shoal (compare blue circles with black curves in Figures 2a and 2b). In every case, the individual H_b of the plunging waves was larger than the local lidar-derived H_s for the same

collection period (compare red with blue circles in Figures 2a and 2b), suggesting that the plunging waves were among the largest waves observed during each collection period.

At the time step closest to the moment the plunging lip intersects with the front face of the wave t_o, the void aspect ratio L_o/W_o ranged from 1.70 to 3.15, with a mean of 2.55 (red vertical line, Figure 3d), similar to the theoretical L_o/W_o of 2.76 (Longuet-Higgins, 1982) (black line, Figure 3d). The observed L_o/W_o are larger than the range (1.46–2.28) in laboratory analyses of plunging breakers over a submerged reef (Blenkinsopp & Chaplin, 2008), but comparable with field observations (1.42–3.43) (Mead & Black, 2001). The void angle from horizontal at t_o (θ_{vo}) correlated weakly with L_o/W_o, with larger (i.e., steeper) θ_{vo} occurring with smaller (i.e., rounder) L_o/W_o ($R^2 = 0.3$, significant at the 99% level, Figure 3d, blue dots). There are stronger relationships between θ_{vo} and the void length normalized by the breaking wave height L_o/H_b, with steeper voids occurring with smaller normalized void lengths ($R^2 = 0.6$, Figure 4c), and between θ_{vo} and the void area normalized by the square of the breaking wave height A_o/H_b^2, with steeper voids occurring with smaller normalized void areas ($R^2 = 0.4$, not shown).

The variability in void shape is illustrated with two waves collected about an hour apart, with L_o/W_o of 2.07 and 2.92 (Figures 4a and 4b, respectively). To investigate the factors contributing to the differences in plunging-wave shapes, L_o/W_o, L_o/H_b, and A_o/H_b^2 were compared with a range of wave-by-wave parameters estimated from the lidar scans and environmental data. Breaking-wave characteristics are influenced by wave properties (primarily wave height and steepness), bathymetry, and wind (Battjes, 1974; Douglass, 1990; Galvin, 1968; Goda, 2010). On planar beaches, breaking type and location often are estimated using the surf-similarity parameter $\beta / (H_b / \lambda_{dw})^{1/2}$ (Battjes, 1974). However, the relevant bottom slope and other breaking parameters in field conditions remain poorly defined (Apotsos et al., 2008; Robertson et al., 2013; Weishar & Byrne, 1978). Additionally, wave breaking over a bar or reef can differ from breaking on a planar slope (Blenkinsopp & Chaplin, 2008; Smith & Kraus, 1991), further complicating analyses of the role of bathymetry in controlling breaking-wave characteristics. Here, the bathymetry differed between the three days of data collection, with wave breaking occurring on a relatively planar slope on September 7 and 8 and over a pronounced bar on October 25 (Figure 1b). The bottom slope between the location of wave breaking and one half of a wavelength offshore had a stronger relationship with void parameters than the slope over one quarter or one full wavelength offshore.

The local bathymetry influenced void shapes, which become rounder (i.e., L_o/W_o decreases) with increasing $\beta_b(k_b h_b)^{1/2}$ ($R^2 = 0.2$, significant at the 98% level, Figure 4g). A similar relationship was found between L_o/W_o and $\beta_b(H_b/\lambda_b)^{1/2}$, with rounder voids occurring on steeper beach slopes and with steeper waves ($R^2 = 0.2$, not shown). Although no relationship was found between L_o/W_o and the surf similarity parameter $\beta_b / (H_b/\lambda)^{1/2}$ (when either the local or deep-water wavelength was used), both A_o/H_b^2 ($R^2 = 0.5$, not shown) and L_o/H_b ($R^2 = 0.5$, Figure 4d) are correlated with the local surf similarity parameter $\beta_b/(H_b/\lambda_b)^{1/2}$.

The normalized void area A_o/H_b^2 also is correlated with both β_b and h_b, with an increase in A_o/H_b^2 on steeper slopes ($R^2 = 0.5$, Figure 4e) and in shallower water ($R^2 = 0.4$, Figure 4f). A similar relationship between the A_o/H_b^2 and the bathymetry was observed in a laboratory, with an increase in A_o/H_b^2 occurring with a decrease in the relative water depth over a submerged reef (h_b/H_{dw}, where H_{dw} is the offshore wave height) (Blenkinsopp & Chaplin, 2008). If the bottom slope is calculated over a full wavelength, β_b is not correlated with A_o/H_b^2 ($R^2 = 0.1$), highlighting the importance of the local bathymetry to wave breaking. Some of the scatter in the relationships between wave shape and environmental parameters may be owing to neglect of alongshore variability in bathymetry that may influence the location and type of wave breaking.

Wave shape (L_o/W_o) is weakly correlated with wind stress τ_w, with offshore-directed (negative) winds decreasing the aspect ratio ($R^2 = 0.2$, Figure 4h). Increased spray off the crest of the waves indicative of strong, opposing winds was visible in many of the lidar scans with small L_o/W_o (Figure 4a). Cross-shore winds influence the breaking type and location in both the laboratory (Douglass, 1990; King & Baker, 1996) and the field (Galloway et al., 1989), with offshore (onshore) winds resulting in an increase in plunging (spilling) breakers and an onshore (offshore) displacement of the breaking location. Onshore-directed winds also alter the shape of waves during the shoaling process (Feddersen & Veron, 2005; Zdyrski & Feddersen, 2021). However, wind effects often are excluded from analyses of breaking-wave shapes. Although a

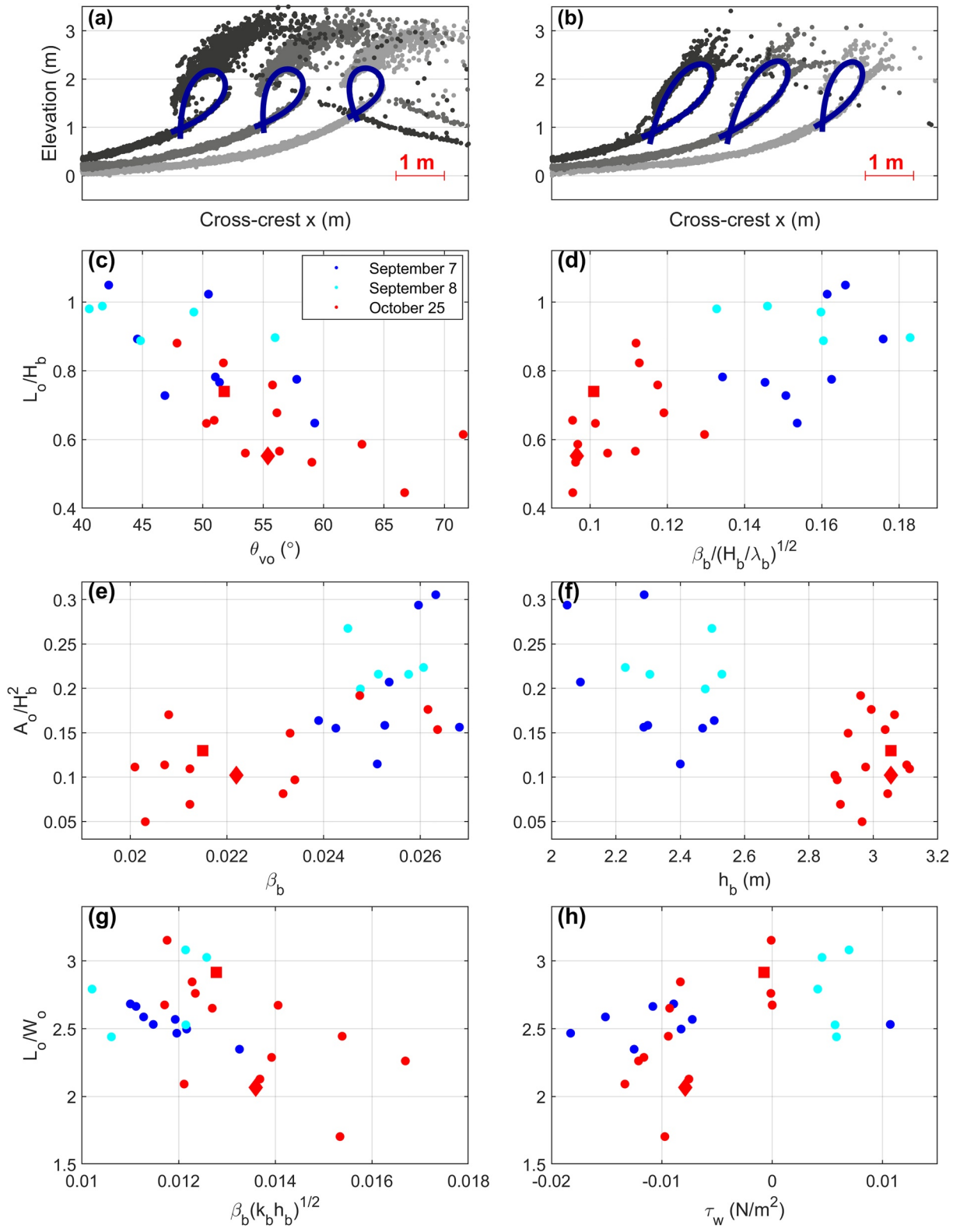

Figure 4. Sea-surface elevation versus cross-crest location showing three frames from two waves with different void shapes on October 25, 2017 at (a) 13:25 UTC (small aspect ratio) and (b) 14:32 UTC (large aspect ratio), along with L_o/H_b as a function of (c) θ_{vo} and (d) $\beta_b/(H_b/L_b)^{1/2}$; A_o/H_b^2 as a function of (e) β_b and (f) h_b; and L_o/W_o as a function of (g) $\beta_b(k_b h_b)^{1/2}$ and (h) τ_w. The waves shown in panels (a), (b) are indicated with a diamond (13:25 UTC) and a square (14:32 UTC) in panels (c–h). In panels (a), (b) subsequent frames have been shifted by 1 m in the cross-crest direction to prevent overlap between frames.

weak relationship between wind stress and wave shape was observed, the present analysis may be limited by the distance (429–544 m) between the lidar data collection in the surf zone and the wind measurements at the end of the pier. Further work is necessary to understand and quantify the role of wind stress in controlling plunging-wave shapes.

The high temporal resolution of the lidar scans allows for analyses of the spatio-temporal evolution of the void shape beyond t_o. In general, the voids were rounder (i.e., smaller aspect ratio) and steeper (i.e., larger void angle from horizontal) as the plunging lip first intersected the front face of the wave, becoming more elongated and less steep through the breaking process (Figures 3c, 3d, 4a and 4b). These changes in void shape and steepness occurred rapidly over 1–3 m and within half a second of t_o. The aspect ratios ranged from 1.7 to 5.0, and the void angles from horizontal ranged from 32° to 72° Figure 3d).

The geometric, kinematic, and dynamic properties of breaking waves influence the rate and location of wave-energy dissipation in the surf zone, which has implications for nearshore circulation, air-sea gas exchange, and sediment transport. The three-dimensional scans of the water surface presented here allowed for analyses of breaking-wave shapes at unprecedented spatial and temporal resolution in an effort to quantify the variability in void shapes and the spatio-temporal evolution of void shape during the early stages of breaking.

Data Availability Statement

The environmental and lidar data can be downloaded from chlthredds.erdc.dren.mil/thredds/catalog/frf/catalog.html and chlthredds.erdc.dren.mil/thredds/catalog/frf/projects/WaveShape/lidarWaveScans/catalog.html.

Acknowledgments
We thank Nicholas Spore, Jason Pipes, Patrick Dickhudt, Spicer Bak, and the staff of the ERDC Field Research Facility for helping to obtain the observations in difficult conditions, and Preston Hartzell and Andrea Albright for helping to process the raw lidar data. Funding was provided by the U.S. Department of Defense (DoD) Laboratory University Collaboration Initiative program, the U.S. Army ERDC Military Engineering Basic Research Program from the Assistant Secretary of the Army for Acquisition, Logistics, and Technology, the Vannevar Bush Faculty Fellowship program, the National Science Foundation, and the U.S. Coastal Research Program. This project was supported in part by an appointment to the Research Participation Program at the DoD, administered by the Oak Ridge Institute for Science and Education through an interagency agreement between the U.S. Department of Energy and the DoD. Opinions, interpretations, conclusions, and recommendations are those of the authors and are not necessarily endorsed by the U.S. Army or DoD.

References

Aagaard, T., Hughes, M. G., & Ruessink, G. (2018). Field observations of turbulence, sand suspension, and cross-shore transport under spilling and plunging breakers. *Journal of Geophysical Research: Earth Surface*, *123*(11), 2844–2862. https://doi.org/10.1029/2018jf004636

Apotsos, A., Raubenheimer, B., Elgar, S., & Guza, R. (2008). Testing and calibrating parametric wave transformation models on natural beaches. *Coastal Engineering*, *55*(3), 224–235. https://doi.org/10.1016/j.coastaleng.2007.10.002

Battjes, J. (1974). Surf similarity. In *Proceedings of the 14th International conference on coastal engineering, Copenhagen, Denmark*. (pp. 466–480). https://doi.org/10.1061/9780872621138.029

Battjes, J. (1988). Surf-zone dynamics. *Annual Review of Fluid Mechanics*, *20*(1), 257–291. https://doi.org/10.1146/annurev.fl.20.010188.001353

Beach, R. A., & Sternberg, R. W. (1996). Suspended-sediment transport in the surf zone: Response to breaking waves. *Continental Shelf Research*, *16*(15), 1989–2003. https://doi.org/10.1016/0278-4343(96)00029-5

Birkemeier, W. A., & Mason, C. (1984). The CRAB: A unique nearshore surveying vehicle. *Journal of Surveying Engineering*, *110*(1), 1–7. https://doi.org/10.1061/(asce)0733-9453(1984)110:1(1)

Blenkinsopp, C., & Chaplin, J. (2007). Void fraction measurements in breaking waves. *Proceedings of the Royal Society A: Mathematical, Physical & Engineering Sciences*, *463*, 3151–3170. https://doi.org/10.1098/rspa.2007.1901

Blenkinsopp, C., & Chaplin, J. (2008). The effect of relative crest submergence on wave breaking over submerged slopes. *Coastal Engineering*, *55*(12), 967–974. https://doi.org/10.1016/j.coastaleng.2008.03.004

Blenkinsopp, C., Mole, M., Turner, I., & Peirson, W. (2010). Measurements of the time-varying free-surface profile across the swash zone obtained using an industrial lidar. *Coastal Engineering*, *57*(11–12), 1059–1065. https://doi.org/10.1016/j.coastaleng.2010.07.001

Brodie, K. L., Raubenheimer, B., Elgar, S., Slocum, R. K., & McNinch, J. E. (2015). Lidar and pressure measurements of inner-surfzone waves and setup. *Journal of Atmospheric and Oceanic Technology*, *32*(10), 1945–1959. https://doi.org/10.1175/jtech-d-14-00222.1

Chanson, H., & Jaw-Fang, L. (1997). Plunging jet characteristics of plunging breakers. *Coastal Engineering*, *31*(1–4), 125–141. https://doi.org/10.1016/s0378-3839(96)00056-7

Douglass, S. L. (1990). Influence of wind on breaking waves. *Journal of Waterway, Port, Coastal, and Ocean Engineering*, *116*(6), 651–663. https://doi.org/10.1061/(asce)0733-950x(1990)116:6(651)

Feddersen, F., & Veron, F. (2005). Wind effects on shoaling wave shape. *Journal of Physical Oceanography*, *35*(7), 1223–1228. https://doi.org/10.1175/jpo2753.1

Flick, R. E., Guza, R. T., & Inman, D. L. (1981). Elevation and velocity measurements of laboratory shoaling waves. *Journal of Geophysical Research: Oceans*, *86*(C5), 4149–4160. https://doi.org/10.1029/jc086ic05p04149

Forte, M. F., Birkemeier, W. A., & Mitchell, J. R. (2017). *Nearshore survey system evaluation (Tech. Rep.)*. ERDC-CHL Vicksburg.

Galloway, J., Collins, M., & Moran, A. (1989). Onshore/offshore wind influence on breaking waves: An empirical study. *Coastal Engineering*, *13*(4), 305–323. https://doi.org/10.1016/0378-3839(89)90039-2

Galvin, C. J. (1968). Breaker type classification on three laboratory beaches. *Journal of Geophysical Research*, *73*(12), 3651–3659. https://doi.org/10.1029/jb073i012p03651

Goda, Y. (2010). Reanalysis of regular and random breaking wave statistics. *Coastal Engineering Journal*, *52*(1), 71–106. https://doi.org/10.1142/s0578563410002129

Grilli, S. T., Guyenne, P., & Dias, F. (2001). A fully non-linear model for three-dimensional overturning waves over an arbitrary bottom. *International Journal for Numerical Methods in Fluids*, *35*(7), 829–867. https://doi.org/10.1002/1097-0363(20010415)35:7<829::aid-fld115>3.0.co;2-2

Grilli, S. T., & Svendsen, I. A. (1990). Long wave interaction with steeply sloping structures. In *Proceedings of the 22th International conference on coastal engineering* (pp. 1200–1213).
Grilli, S. T., Svendsen, I. A., & Subramanya, R. (1997). Breaking criterion and characteristics for solitary waves on slopes. *Journal of Waterway, Port, Coastal, and Ocean Engineering*, *123*(3), 102–112. https://doi.org/10.1061/(asce)0733-950x(1997)123:3(102)
Inman, D. L., Zampol, J. A., White, T. E., Hanes, D. M., Waldorf, W. B., & Kastens, K. A. (1980). Field measurements of sand motion in the surf zone. *Proceedings of the 17th International conference on coastal engineering, Sydney, Australia*. (pp. 1215–1234). https://doi.org/10.1061/9780872622647.074
Kiger, K. T., & Duncan, J. H. (2012). Air-entrainment mechanisms in plunging jets and breaking waves. *Annual Review of Fluid Mechanics*, *44*, 563–596. https://doi.org/10.1146/annurev-fluid-122109-160724
King, D., & Baker, C. (1996). Changes to wave parameters in the surf zone due to wind effects. *Journal of Hydraulic Research*, *34*(1), 55–76. https://doi.org/10.1080/00221689609498764
Large, W., & Pond, S. (1981). Open ocean momentum flux measurements in moderate to strong winds. *Journal of Physical Oceanography*, *11*(3), 324–336. https://doi.org/10.1175/1520-0485(1981)011<0324:oomfmi>2.0.co;2
Lin, P., & Liu, P. L.-F. (1998). Turbulence transport, vorticity dynamics, and solute mixing under plunging breaking waves in surf zone. *Journal of Geophysical Research: Oceans*, *103*(C8), 15677–15694. https://doi.org/10.1029/98jc01360
Long, C. E., & Oltman-Shay, J. M. (1991). *Directional characteristics of waves in shallow water (Tech. Rep.). USAE waterways experiment station*. Coastal Engineering Research Center.
Longuet-Higgins, M. (1982). Parametric solutions for breaking waves. *Journal of Fluid Mechanics*, *121*, 403–424. https://doi.org/10.1017/s0022112082001967
Longuet-Higgins, M., & Cokelet, E. (1976). The deformation of steep surface waves on water-I. A numerical method of computation. *Proceedings of the Royal Society of London. A. Mathematical and Physical Sciences*, *350*(1660), 1–26. https://doi.org/10.1098/rspa.1976.0092
Longuet-Higgins, M., & Cokelet, E. (1978). The deformation of steep surface waves on water - II. Growth of normal-mode instabilities. *Proceedings of the Royal Society of London. A. Mathematical and Physical Sciences*, *364*(1716), 1–28. https://doi.org/10.1098/rspa.1978.0185
Lubin, P., Vincent, S., Abadie, S., & Caltagirone, J. P. (2006). Three-dimensional large eddy simulation of air entrainment under plunging breaking waves. *Coastal Engineering*, *53*(8), 631–655. https://doi.org/10.1016/j.coastaleng.2006.01.001
Martins, K., Blenkinsopp, C., Deigaard, R., & Power, H. E. (2018). Energy dissipation in the inner surf zone: New insights from lidar-based roller geometry measurements. *Journal of Geophysical Research: Oceans*, *123*(5), 3386–3407. https://doi.org/10.1029/2017jc013369
Martins, K., Blenkinsopp, C. E., Power, H. E., Bruder, B., Puleo, J. A., & Bergsma, E. W. (2017). High-resolution monitoring of wave transformation in the surf zone using a lidar scanner array. *Coastal Engineering*, *128*, 37–43. https://doi.org/10.1016/j.coastaleng.2017.07.007
Mead, S., & Black, K. (2001). Predicting the breaking intensity of surfing waves. *Journal of Coastal Research, SI*, *10*, 51–65.
Nielsen, P. (1984). Field measurements of time-averaged suspended sediment concentrations under waves. *Coastal Engineering*, *8*(1), 51–72. https://doi.org/10.1016/0378-3839(84)90022-x
Peregrine, D. (1983). Breaking waves on beaches. *Annual Review of Fluid Mechanics*, *15*(1), 149–178. https://doi.org/10.1146/annurev.fl.15.010183.001053
Peregrine, D. (1998). Surf zone currents. *Theoretical and Computational Fluid Dynamics*, *10*(1–4), 295–309. https://doi.org/10.1007/s001620050065
Peregrine, D., Cokelet, E., & McIver, P. (1980). The fluid mechanics of waves approaching breaking. In *Proceedings of the 17th International conference on coastal engineering, Sydney, Australia*. (pp. 512–528). https://doi.org/10.1061/9780872622647.032
Robertson, B., Hall, K., Zytner, R., & Nistor, I. (2013). Breaking waves: Review of characteristic relationships. *Coastal Engineering Journal*, *55*(01), 1350002-1–1350002-40. https://doi.org/10.1142/s0578563413500022
Smith, E. R., & Kraus, N. C. (1991). Laboratory study of wave-breaking over bars and artificial reefs. *Journal of Waterway, Port, Coastal, and Ocean Engineering*, *117*(4), 307–325. https://doi.org/10.1061/(asce)0733-950x(1991)117:4(307)
Ting, F. C., & Kirby, J. T. (1994). Observation of undertow and turbulence in a laboratory surf zone. *Coastal Engineering*, *24*(1–2), 51–80. https://doi.org/10.1016/0378-3839(94)90026-4
Ting, F. C., & Kirby, J. T. (1995). Dynamics of surf-zone turbulence in a strong plunging breaker. *Coastal Engineering*, *24*(3–4), 177–204. https://doi.org/10.1016/0378-3839(94)00036-w
Ting, F. C., & Kirby, J. T. (1996). Dynamics of surf-zone turbulence in a spilling breaker. *Coastal Engineering*, *27*(3–4), 131–160. https://doi.org/10.1016/0378-3839(95)00037-2
Vinje, T., & Brevig, P. (1981). Numerical simulation of breaking waves. *Advances in Water Resources*, *4*(2), 77–82. https://doi.org/10.1016/0309-1708(81)90027-0
Voulgaris, G., & Collins, M. (2000). Sediment resuspension on beaches: Response to breaking waves. *Marine Geology*, *167*(1–2), 167–187. https://doi.org/10.1016/s0025-3227(00)00025-6
Weishar, L. L., & Byrne, R. J. (1978). Field study of breaking wave characteristics. In *Proceedings of the 16th International conference on coastal engineering, Hamburg, Germany*. (pp. 487–506). https://doi.org/10.1061/9780872621909.029
Yasuda, T., Mutsuda, H., & Mizutani, N. (1997). Kinematics of overturning solitary waves and their relations to breaker types. *Coastal Engineering*, *29*(3–4), 317–346. https://doi.org/10.1016/s0378-3839(96)00032-4
Zdyrski, T., & Feddersen, F. (2021). Wind-induced changes to surface gravity wave shape in shallow water. *Journal of Fluid Mechanics*, *913*, A27. https://doi.org/10.1017/jfm.2021.15